AN EQUI-DIMENSIONAL FINITE ELEMENT APPROACH FOR FLOW PROBLEMS IN FRACTURED POROUS MEDIA

Marco Favino[1] and Maria Giuseppina Chiara Nestola[2,3]

[1]Institute of Earth Sciences, University of Lausanne, Lausanne, Switzerland, marco.favino@unil.ch
[2] Institute of Computational Sciences , Università della Svizzera Italiana, Lugano, Switzerland , nestom@usi.ch
[3] Institute of Geochemics and Petrology ETH Zurich, Switzerland

February 28, 2021

Abstract

We propose a novel approach for flow simulations in fractured porous media based on an equi-dimensional representation of the fractures and a standard continuous finite element (FE) method. We employ an adaptive mesh refinement strategy to automatically adjust an initial regular mesh to any fracture distribution with a desired accuracy. The proposed approach is easily implementable in any FE software, does not involve the coupling of different discretizations, and provides symmetric and positive definite stiffness matrices. We provide a systematic validation of our method and we show that it can be used to simulate fluid flow for fracture networks of realistic complexity.

Keywords: Fractured porous media; Adaptive mesh refinement; Fluid flow; Finete element method

1 INTRODUCTION

The numerical simulation of fractured porous media is relevant for many applications in the Earth, environmental, and engineering applications, such as geothermal energy production, hydrocarbon exploration, nuclear waste disposal, CO_2 storage. Fractures are heterogeneities characterized by 1) material properties which are highly different with respect to the ones of the embedding background and 2) one dimension, usually referred to as aperture, that is much smaller compared to the other ones.

The geometric complexity of realistic fracture networks and the multiple length scales involved pose several difficulties to the numerical simulation of fractured media. In particular, for models based on an equi-dimensional representation of the fractures, i.e., models in which the fractures have the same dimension of the embedding background, the generation of meshes is one of the major challenges. This finds its expression in the fact that the use of equi-dimensional models have so far been limited to small numbers of the fractures [6, 14, 5]. Among the methods based on an equi-dimensional

representation, the mimetic finite difference (MFD) is the most successful one, as it is robust even on anisotropic and distorted meshes [1].

To overcome such difficulties, discrete fracture-matrix (DFM) approaches allow for a hybrid-dimensional representation of the fractures, i.e., fractures are considered objects of one dimension less than the embedding background. In DFM approaches, the same model is simulated in the fracture and in the background domains and suitable terms are introduced to couple the two models. Hence, the arising stiffness matrices present a block structure. Several conforming and non-conforming discretization methods, based on finite volume (FV) and finite element (FE) methods, have been proposed for the DFM approach.

Among the conforming methods, we name the BOX, which is a vertex-centered FV method [8], the TPFA, which is a control-volume finite difference method which uses a two-point flux approximation [11], the MPFA, which is a generalization of the former and employs a multi-point flux approximation [17]. Among the non-conforming methods, we name the embedded discrete fracture-matrix (EDFM) [13], the extended finite elements (XFEM) [12], and methods base on mortar-type techniques [3].

Although hybrid-dimensional representations partially simplify the process of mesh creation, conforming methods still require meshes that match at the intersections and the mesh generation still remains an issue for cases of high geometrical complexity. On the other hand, non-conforming methods provide more freedom in the mesh generation, as the fracture mesh can be located arbitrarily inside the background domain. However, in general, they are not straightforward to implement and may present high condition numbers, when the fracture grid cuts the background elements in small subelements. Moreover, hybrid-dimensional models rely on the assumption of negligible aperture. However, fracture apertures which are two-orders-of-magnitude less than the background size are often encountered [10, 5, 2]. In these cases, the assumption of negligible aperture is not applicable and the error coming from the lower-dimensional representation of the fractures may dominate the discretization error.

In this work, we present an alternative approach based on an equi-dimensional representation of the fractures and a continuous FE method on adapted meshes that allows to simulate fractured media of realistic complexity. Employing an idea similar to the one presented in [4], we use an adaptive mesh refinement (AMR) strategy to create a hierarchy of meshes that approximate the interfaces between the fractures and the embedding background with increasing accuracy without the need to explicitly resolve them. Starting from an initial regular mesh unrelated to the fracture distribution, at each step of the AMR strategy, we create a new mesh level by refining the elements which have non-empty overlap with the interfaces between fractures and background.

We employ this approach for the simulation of single-phase fluid flow problems and we validate it using the four tests proposed in the seminal *benchmark paper* for single-phase flow in fractured porous media [5]. We show that a reasonable number of AMR steps allows to reproduce the fundamental characteristics of the solutions of all the proposed tests. As the proposed approach is based on standard continuous FE method and does not involve coupling terms, it can be easily implemented in any FE framework, the condition number does not suffer for elongated or distorted elements, and the resulting stiffness matrix is suitable for the solution with efficient algebraic multigrid method. Moreover, our approach can be employed for the computation of reference solutions of models with equi-dimensional representations of the fractures in the process

of validating hybrid-dimensional representations in complicated and realistic fracture networks.

This work is organized as follows. In Section 2, we introduce the flow problem and the FE discretization of adapted meshes. In Section 3, we discuss the AMR strategy. In Section 4, we report the results of the validation of our method. Finally, we offer some concluding remarks in Section 5.

2 MATHEMATICAL PRELIMINARIES

We present the mathematical model and the FE discretization in a two-dimensional setting. The approach discussed below can be straightforwardly extended to three-dimensional settings.

2.1 Geometrical definitions

We denote a polygonal domain in the Euclidean space $\mathscr{E}^2$ by Ω. The boundary of Ω is $\partial\Omega$ and the outward normal to Ω is $\underline{n}$. In case of an axis-aligned rectangular domains, we employ the symbol Ω^L and the two dimensions of the domain are denoted by L_x and L_y. We introduce a set $\mathcal{F}$ of rectangular inclusions $f^i \subset \Omega$ with $i = 1,2 \dots N_f$, where $N_f = |\mathcal{F}|$ is the number of inclusions. We define the background and inclusions subset of Ω, respectively, by

$$\Omega_f := \overline{\bigcup_{i=1}^{N_f} f^i} \quad \text{and} \quad \Omega_b := \overline{\Omega \backslash \Omega_f}.$$

Both Ω_b and Ω_f may be non-connected sets. The set $\Gamma := \overline{\Omega}_b \cap \overline{\Omega}_f$ is the interface between the background and the fracture subdomains.

2.2 The model problem

We assume $\partial\Omega$ can be decomposed into Γ_D and Γ_N, i.e., respectively, the subsets where Dirichlet and Neumann boundary conditions are imposed. Dirichlet boundary conditions are denoted by p_D and Neumann boundary conditions by q_N. Neglecting source terms, the weak formulation of single-phase flow in porous media reads

$$\text{Find } p \in U \text{ such that } \quad \int_\Omega k \nabla p \cdot \nabla q \, \mathrm{d}\Omega = \int_{\Gamma_N} q_N v \, \mathrm{d}\Gamma \quad \forall v \in V, \tag{1}$$

where p is the pressure, $V = \{v \in H^1(\Omega) : v|_{\Gamma_D} = 0\}$, and $U = \{v \in H^1(\Omega) : v|_{\Gamma_D} = p_D\}$. The permeability k attains different values in Ω_b and Ω_f, i.e.,

$$k = \begin{cases} k_b, & \text{in} \quad \Omega_b, \\ k_f, & \text{in} \quad \Omega_f. \end{cases}$$

Existence, uniqueness, and stability results for the weak problem (1) follow from Lax-Milgram theorem.

Close to the vertices of the inclusions, usually referred to as singular points, the solution p can be written as the sum of a regular function in $H^2(\Omega)$ and some singular functions [7, 16]. Such singular functions reduce the regularity of solution. For example, we report one of the well-known regularity results from [15], which states that

Theorem 1 *The solution of problem* (1) *fulfills* $p \in H^{1+1/4}(\Omega)$.

Hence, due to the discontinuities in k, the regularity of the solution is reduced and classical smooth solutions to (1) are not defined.

2.3 Finite element approximation

To discretize Eq. (1), we employ a standard conforming FE method defined on non-conforming meshes. Meshes are locally refined close to the interface but they do not resolve the interface Γ. We refer to these kinds of meshes as unresolved or unfitted. Due to the use of unresolved meshes, material properties may be discontinuous over the elements of the mesh that are crossed by the interface. Corresponding material properties are assigned to the quadrature point during the assembly. Due to this lack of regularity, we employ a composite quadrature rule with one node per sub-element and 10^2 sub-elements per mesh element.

The discretization of the weak formulation (1) results in a linear system of the form

$$\mathbf{A}\mathbf{p} = \mathbf{f}, \tag{2}$$

where the stiffness matrix $\mathbf{A}$ is symmetric and positive definite. We remind that due to Theorem 1, convergence of the FE method could be suboptimal for such a problem, as it requires that the solution belong to be in $H^2(\Omega)$ to ensure at least a convergence of order one in energy norm.

3 ADAPTIVE MESH REFINEMENT FOR EQUI-DIMENSIONAL INCLUSIONS

We briefly describe the AMR strategy for the generation of adapted equi-dimensional meshes for arbitrary fracture networks. We follow the strategy presented in [4] even if we employ a different criterion to choose the elements to refine. Such an approach has been used for the simulation of hydro-mechanical coupling in fractured porous media in [9, 18].

We consider meshes that are non-conforming tessellations of Ω with elements K. Hence, we assume that a mesh can have hanging vertices, i.e., there could exist a vertex of an element K_i that may belong to an edge of another element K_j. We restrict ourselves to the case of 1-irregular (or balanced) meshes, for which at most one hanging node can exist per edge.

We denote the initial regular mesh by $\mathcal{T}^0$. Denoting by N_x the number of elements along one direction, we employ the symbol $\mathcal{T}^0_{N_x}$ to stress the resolution of the initial mesh. By red-refinement, we refer to the split of a parent element into four identical child elements. An adapted mesh $\mathcal{T}^\ell$ (or $\mathcal{T}^\ell_{N_x}$), with $\ell > 1$ is obtained by red-refining a subset $\mathcal{A}$ of elements of $\mathcal{T}^{\ell-1}$ (or $\mathcal{T}^{\ell-1}_{N_x}$). We denote by $h^\ell_{N_x} = L_x/N_x/2^\ell$ the size of the smallest edge present in the mesh $\mathcal{T}^\ell_{N_x}$.

In order to construct the mesh $\mathcal{T}^\ell$ from $\mathcal{T}^{\ell-1}$, we add the elements of $\mathcal{T}^{\ell-1}$ that intersect the interface Γ to the set $\mathcal{A}$. Then, we add all the elements that are needed to ensure that $\mathcal{T}^\ell$ is 1-irregular. Finally, we replace the elements in $\mathcal{A}$ with their red-refinement.

Figure 1 shows some steps of the AMR strategy for a unitary square with two fractures. The domain, reported Subfigure 1a, contains two fractures, which are centered

in $(0.5, 0.5)$, have length of 0.8, and have an aperture of 0.05. We on purpose consider thick fractures to visualize the adaptive steps. The skewed one is inclined of an angle of 30°. In Figure 1b, we report an initial mesh $\mathcal{T}_{10}^0$. In Figures 1c-1h, we report the hierarchy of adapted meshes created with the AMR strategy. We observe how in the first three steps, all elements which are in the interior of the fracture are refined. Later, in the steps from 3 to 6, the refinement is performed only on close to the boundary. After six steps, the mesh size is $h_{10}^6 = 1/10/2^6 \approx 1.5 \times 10^{-3}$.

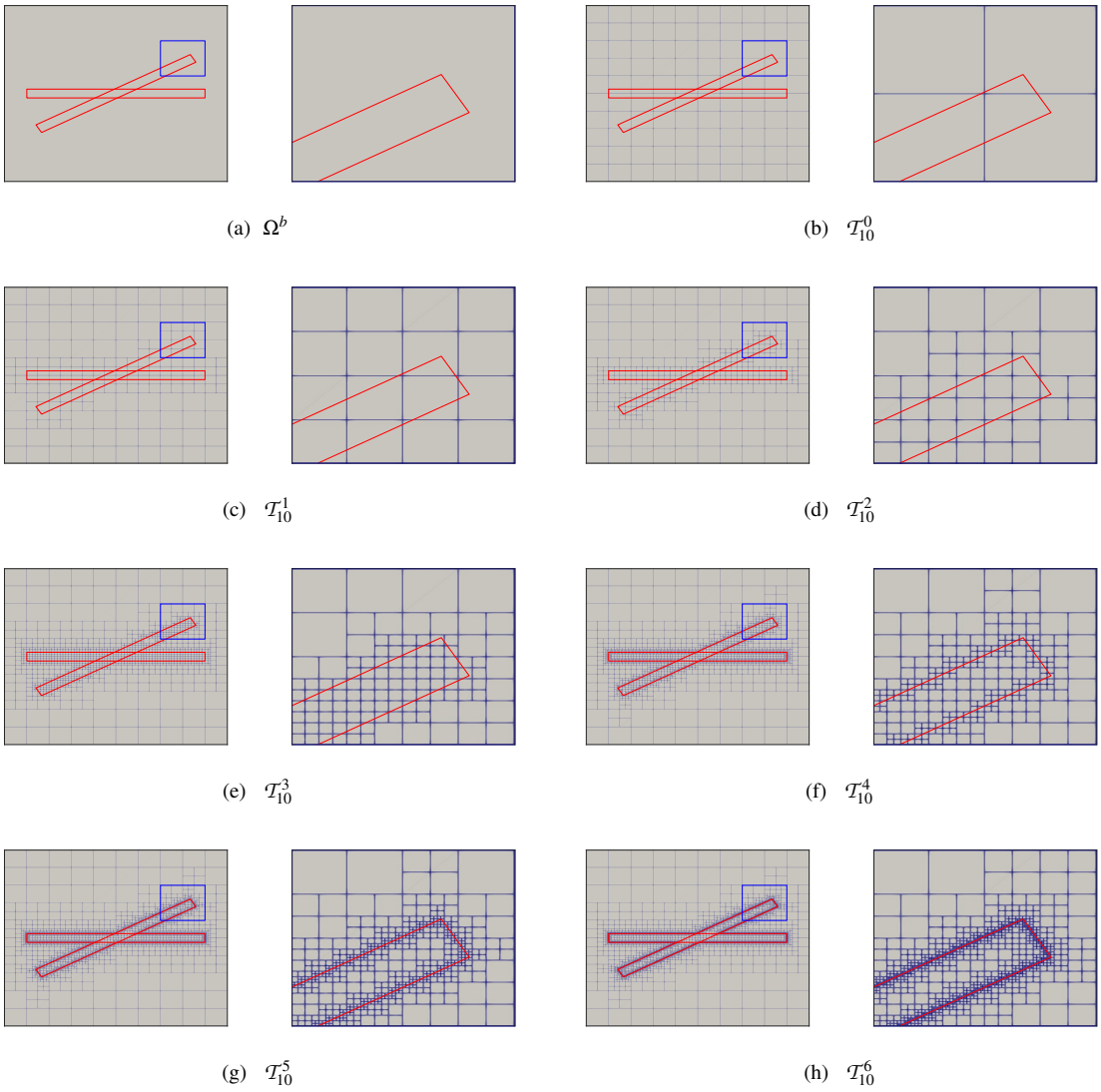

(a) Ω^b (b) $\mathcal{T}_{10}^0$

(c) $\mathcal{T}_{10}^1$ (d) $\mathcal{T}_{10}^2$

(e) $\mathcal{T}_{10}^3$ (f) $\mathcal{T}_{10}^4$

(g) $\mathcal{T}_{10}^5$ (h) $\mathcal{T}_{10}^6$

Figure 1: (a) Unitary square domain containing two fractures (red) intersecting each other at an angle of 30°. The blue rectangle denotes the fracture tip, for which blowups are shown on the right of each subfigure. (b) Initial regular mesh. (c)-(h) Adapted meshes created at steps from 1 to 6 of the AMR strategy.

4 NUMERICAL RESULTS

We validate the described approach using the tests proposed in the benchmark paper [5]. This work presents

- four tests for single-phase fluid flow in fractured porous media featuring fracture networks of different complexity intended to be benchmarks for discretization approaches;
- a comparison of the results obtained with different discretization approaches. The considered approaches are all based on hybrid-dimensional formulations, except one based on an equi-dimensional formulation and a mimetic finite difference (MFD) method.

Following the nomenclature of the benchmark paper, we refer to the four tests with the names: 1) regular fracture network, 2) Hydrocoin, 3) complex fracture network, 4) realistic fracture network. For problem 1), two cases are considered: a conductive network, featuring fractures with a permeability larger than the one of the background, and a blocking network, featuring fractures with a permeability much smaller than the one of the background. We refer to the conductive and blocking cases with 1c) and 1b), respectively. For problem 3), two cases are considered: a vertical flow (top to bottom) and a horizontal flow (left to right). We refer to the vertical and horizontal cases with 3v) and 3h), respectively.

Tests 1), 3), 4) are defined in axis-aligned domain Ω^L and, hence, a structured initial mesh is employed. Test 2) is defined in a polygonal domain and an initial mesh has been created with Cubit 13.1.

As proposed in the benchmark paper, we analyze the pressure profiles along some segments. For tests 1), 2), 3), we compare our solutions against the reference one computed with an equi-dimensional MFD method. Instead for problem 4), we compare our solutions against the solutions obtained with the hybrid-dimensional approaches.

Simulations have been performed with `parrot2`, a software applications implemented in the FE framework MOOSE. The arising linear system has been solved using the algebraic multigrid solver `Hypre BoomerAMG` for tests 1), 2) 3). For test 4), the linear system has been solved using the parallel direct solver `Mumps`.

4.1 Regular fracture network

The first test consists of a regular fracture network of six fractures embedded in a unitary square. Fracture aperture is 10^{-4} m, i.e., four-orders-of-magnitude less than the domain size. In Figure 2, we report an example of the adapted meshes resulting by the application of the AMR strategy: an initial mesh with $N_x = N_y = 40$ is reported in Figure 2a, while the adapted meshes resulting after 6 AMR steps is reported in Figure 2b. We observe how all elements overlapping with the boundary of one fracture, which is modeled as a rectangle, are gradually refined to improve the resolution. This illustrates the effectiveness of the meshing algorithm. Figures 2c and 2d reports the spatial pressure distribution for the conductive and blocking cases, respectively, computed on the mesh $\mathcal{T}^8_{160}$.

For the conductive case, the analysis is performed along the horizontal ($y = 0.7$) and vertical ($x = 0.5$) dashed black segments reported in Figure 2a. For the blocking case, the analysis is performed along the diagonal dashed black segment.

For the conductive case, the pressure profiles computed along the horizontal and vertical segments are reported in Figures 2e and 2f, respectively, for different mesh sizes of the initial mesh and different number of AMR steps. From Figure 2e, we observe that our approach is able to correctly reproduce the pressure profile along the horizontal segment even for coarse meshes. Instead, for what concerns the vertical line (2f), we observe that the results are mostly dominated by the minimum mesh size. In particular, a value of $h^{\ell}_{N_x} = 1/40/2^{11}$ provides a pressure profile that coincides with the reference one. These results are confirmed also by additional numerical simulations performed on denser meshes that we are not reported.

For the blocking case, the pressure profiles are reported in Figure 2g. We observe that our approach based on a continuous FE method and an equi-dimensional formulation is able to reproduce the correct pressure profiles even for coarse meshes. This result is particularly interesting, as some methods based on continuous FE, but hybrid-dimensional formulations (BOX and EDFM), were not able to capture the pressure discontinuities. Again, as for the vertical segment in the conductive case, we observe that there exists a threshold value for the minimum mesh size in order to obtain results that are superimposed with the reference solution. Such a value is $h^{\ell}_{N_x} = 1/40/2^{12}$.

As a result of this first analysis, we can conclude that the our approach based on an equi-dimensional formulation and continuous FE is able to reproduce the correct pressure distribution, if the interfaces are approximated with a sufficient accuracy. Such accuracy may depend on the material properties of the background and of the fractures.

4.2 Hydrocoin

This test was proposed within the international Hydrocoin project, (Swedish Nuclear Power Inspectorate (SKI). The original domain has been slightly modified according to the description provided in [5]. The aperture of the fractures is about 10^1 m, i.e., two-orders-of-magnitude less than the domain size.

The initial mesh, reported in Figure 3a, is quite coarse and is characterized by $N_x = 12$ and $N_y = 9$. In such a figure, we have superimposed the two inclined fractures of this test and the horizontal segment along which the analysis is performed . The adapted mesh after six steps of AMR is reported in Figure 3b. The resulting adapted mesh is characterized by an $h^6_{12} \approx 2$, meaning that roughly five elements fit in the fracture aperture. Figure 3c depicts the spatial distribution of the pressure on such a mesh.

Figure 3d reports the pressure profile computed along the horizontal line (y =-200 m) for different steps of AMR. As for the first test, increasing of the number of AMR steps allows to obtain solutions which are perfectly superimposed with the reference one. For this test, such a characteristic has not been observed for discretizations based on hybrid-dimensional formulations. This is due to the fact that hybrid-dimensional formulation relies on the assumption of negligible aperture that is not justified for fractures that are so large.

4.3 Complex fracture network

This test features a unitary square with ten fractures distributed as in Figure 4a. Eight fractures, depicted in red, are conductive and two fractures, depicted in blue, are blocking. A resulting adapted mesh after 5 steps of AMR is reported in Figure 4b. At the

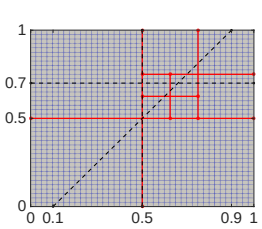

(a) $\mathcal{T}_{40}$

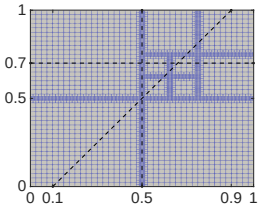

(b) $\mathcal{T}_{40}^{6}$

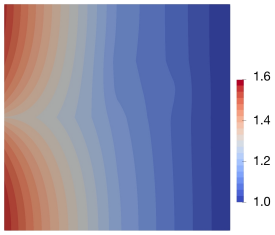

(c) Pressure Conductive

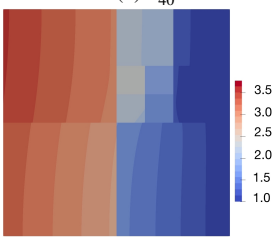

(d) Pressure Blocking

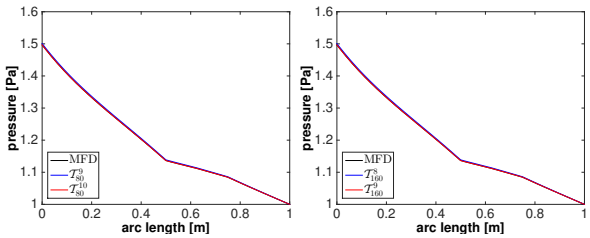

(e) Conductive case: horizontal line

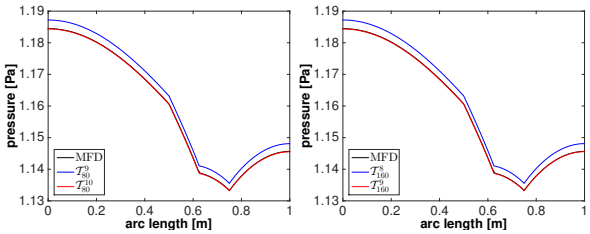

(f) Conductive case: vertical line

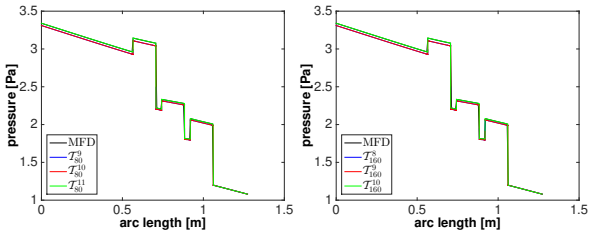

(g) Blocking case

Figure 2: (a) Initial regular mesh where we depict the fracture network in red. (b) Adapted mesh obtained after six AMR steps. (c)-(d) Pressure distribution for the conductive and the blocking case, respectively. (e-f) Solutions are evaluated along the back segments for the conductive case. (g) Solutions evaluated along the back segments for blocking case.

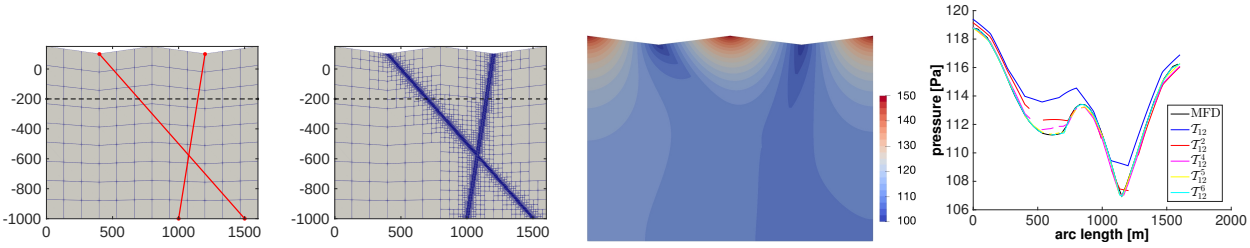

(a) $\mathcal{T}_{12}$ (b) $\mathcal{T}_{12}^{6}$ (c) Pressure distribution (d) Pressure profiles at y =-200

Figure 3: (a) Initial regular mesh where we depict the fractures in red. (b) Adapted mesh obtained after six AMR steps. (c) Pressure distribution. (d) Pressure profiles evaluated along the black segment.

quadrature points belonging to more than one fracture, the assigned permeability is the harmonic mean of the permeabilities of each fracture.

In Figures 4c and 4c, we report the pressure distribution for the vertical and horizontal flow cases, respectively. These pressure distributions resemble the ones reported in the benchmark paper.

The pressure profiles are evaluated along the black segment reported in Figure 4a. In Figures 4e and 4f, we report the pressure profiles for the vertical flow case. In Figures 4g and 4h, we report the pressure profiles for the horizontal flow case. For all the results, we observe that the error is always dominated by the accuracy with which the fractures boundary are resolved and almost no influence is given by the initial background mesh. As also observed in [5], the vertical flow is approximated more easily. Conversely, for the horizontal flow, finer meshes are necessary. Again, our approach, even though continuous, is able to reproduce the pressure drop close to the blocking fractures.

4.4 Realistic fracture network

This final test features a realistic network of 63 fractures of different length. The aperture is four-orders-of-magnitude less than background size. The conductivity of the fractures is six-orders-of-magnitude larger than the one of the background. For this test, we start from a coarse mesh with $N_x = 7$ and $N_y = 6$. This initial mesh is reported in Figure 5a as well as the horizontal and the vertical segments, along which the solution is evaluated. The meshes after three and five AMR steps are reported in Figures 5b and 5c, respectively. In total, we apply to this mesh up to 10 AMR steps. The mesh $\mathcal{T}_7^{10}$ is characterized by a value $h_7^{10} \approx 10^{-2}$, that coincides with the fracture aperture. The resulting pressure distribution is illustrated in Figure 5d. For this test, no reference solution based on equi-dimensional representations has been provided, due to the difficulties in the generation a mesh that is able to resolve the intersections and the interfaces between the background and the embedded fractures. For this reason, we perform a comparison against all the solutions reported in [5] and based on hybrid-dimensional models. We observe that the pressure profiles obtained with our approach are in agreement with the published solutions along the two proposed segments, (Figures 5e and 5f). In particular, our approach is able to reproduce all the features of the

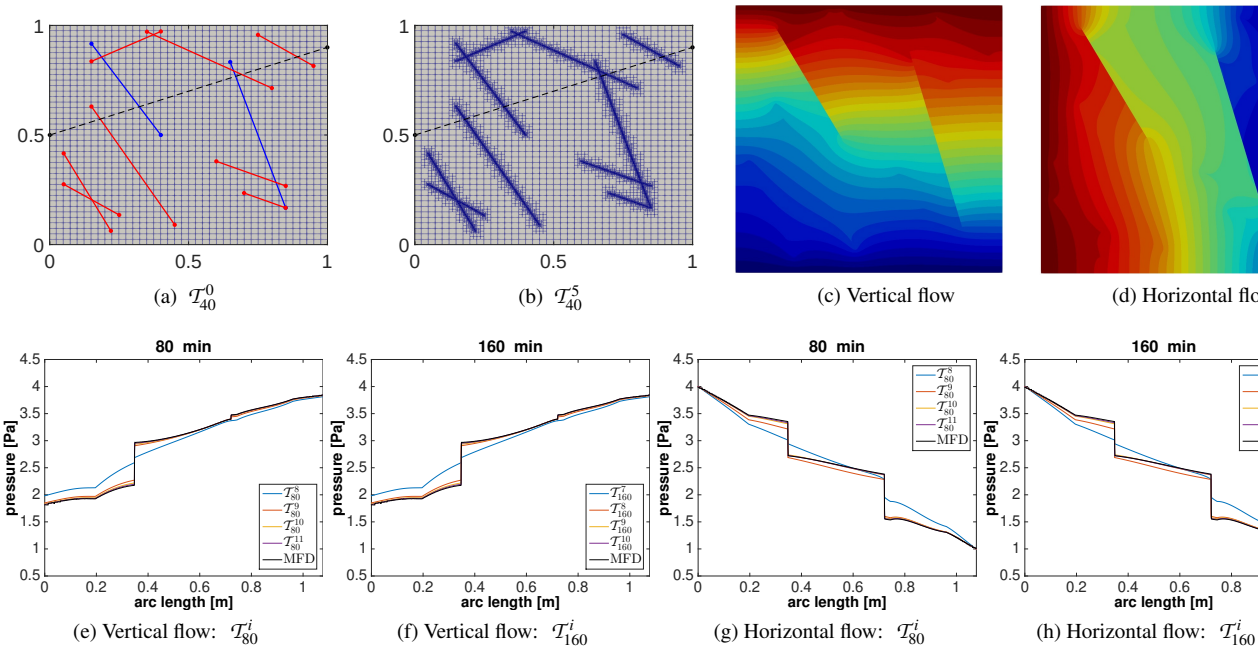

(a) $\mathcal{T}^0_{40}$ (b) $\mathcal{T}^5_{40}$ (c) Vertical flow (d) Horizontal flo

(e) Vertical flow: $\mathcal{T}^i_{80}$ (f) Vertical flow: $\mathcal{T}^i_{160}$ (g) Horizontal flow: $\mathcal{T}^i_{80}$ (h) Horizontal flow: $\mathcal{T}^i_{160}$

Figure 4: (a) Initial regular mesh where we depict the conductive fractures in red and the blocking fractures in blue. (b) Mesh obtained after five AMR steps. (c) Pressure distribution for the vertical flow. (d) Pressure distribution for the horizontal flow. (e)-(h) Pressure profiles evaluated along the black dashed segment depicted in (a).

solution along these two segments.

5 CONCLUSIONS

We have proposed an approach for the simulation of fluid flow in fractured porous media based on an equi-dimensional representation of the fractures and a continuous FE method. The equi-dimensional representation of the fractures allows to consider the full physics occurring in the fracture, i.e., to include cross-fracture phenomena, which are usually neglected in hybrid-dimensional representations. In order to create suitable meshes for fractured media, we employed an adaptive mesh refinement strategy, which allows, starting from a regular initial mesh, to refine the element close to interfaces between fractures and the embedding background. In this way, we can adapt any initial mesh to approximate even the more complicated fracture distribution with a desired accuracy. As our approach does not require any coupling between different geometrical entities, it can be directly implemented in any FE framework. Moreover, it provides provides linear systems characterized by a stiffness matrix which is symmetric and positive definite. Hence, the solution can be realized with efficient algebraic multigrid solvers.

We have validated our approach using the tests proposed in the seminal benchmark paper for single-phase fluid flow. We showed that our method is able to correctly reproduce all the pressure profiles and that the accuracy with which the fractures are

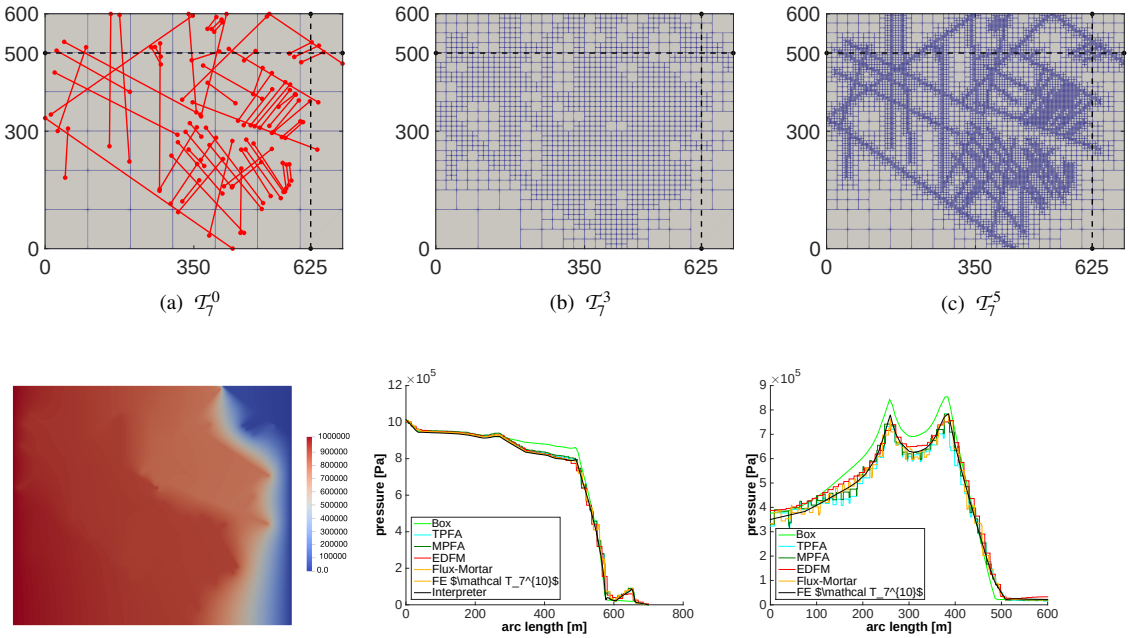

(a) $\mathcal{T}_7^0$ (b) $\mathcal{T}_7^3$ (c) $\mathcal{T}_7^5$

(d) Pressure distribution (e) Horizontal segment (f) Vertical segment

Figure 5: (a) Initial regular mesh where we depict the fractures in red. (b) Adapted mesh obtained after three AMR steps. (c) Adapted mesh obtained after five AMR steps. (d) Pressure distribution. (e) Pressure profiles evaluated along the horizontal black dashed segment depicted in (a). (f) Pressure profiles evaluated along the vertical black dashed segment depicted in (a).

approximated is the fundamental criterion to obtain correct results. This aspect is much more relevant than the accuracy of the background mesh.

Although the proposed method has shown to be able to reproduce all the pressure profiles proposed in the several tests, the accuracy depends on the fracture aperture, the conductivity, the geometry, the segment along which the numerical solutions are evaluated. For geometries for which a reference solution does not exist, a possible strategy would be to evaluate two solutions computed on meshes obtained from subsequent application of our AMR strategy. However, the use of error estimators for interface problems would provide a more sound strategy in the choice of the mesh.

Finally, we would like to point out that the proposed approach can be employed to compute reference solutions with equi-dimensional formulations in order to evaluate the accuracy and the approximation properties of methods based on hybrid-dimensional formulations.

ACKNOWLEDGEMENTS

Marco Favino acknowledges gratefully the support of the Swiss National Science Foundation (SNSF) through the grant PZ00P2_180112. Maria GC Nestola acknowledges

gratefully the project "Forecasting and Assessing Seismicity and Thermal Evolution in geothermal Reservoirs" (FASTER) founded by Platform for Advanced and Scientific Computing (PASC).

References

[1] Paola F Antonietti, Luca Formaggia, Anna Scotti, Marco Verani, and Nicola Verzott. Mimetic finite difference approximation of flows in fractured porous media. *ESAIM: Mathematical Modelling and Numerical Analysis*, 50(3):809–832, 2016.

[2] Inga Berre, Wietse M. Boon, Bernd Flemisch, Alessio Fumagalli, Dennis Gläser, Eirik Keilegavlen, Anna Scotti, Ivar Stefansson, Alexandru Tatomir, Konstantin Brenner, Samuel Burbulla, Philippe Devloo, Omar Duran, Marco Favino, Julian Hennicker, I-Hsien Lee, Konstantin Lipnikov, Roland Masson, Klaus Mosthaf, Maria Giuseppina Chiara Nestola, Chuen-Fa Ni, Kirill Nikitin, Philipp Schädle, Daniil Svyatskiy, Ruslan Yanbarisov, and Patrick Zulian. Verification benchmarks for single-phase flow in three-dimensional fractured porous media. *Advances in Water Resources*, 147:103759, 2021.

[3] Wietse M Boon, Jan M Nordbotten, and Ivan Yotov. Robust discretization of flow in fractured porous media. *SIAM Journal on Numerical Analysis*, 56(4):2203–2233, 2018.

[4] Marco Favino, Jürg Hunziker, Eva Caspari, Beatriz Quintal, Klaus Holliger, and Rolf Krause. Fully-automated adaptive mesh refinement for media embedding complex heterogeneities: application to poroelastic fluid pressure diffusion. *Computational Geosciences*, 24(3):1101–1120, 2020.

[5] Bernd Flemisch, Inga Berre, Wietse Boon, Alessio Fumagalli, Nicolas Schwenck, Anna Scotti, Ivar Stefansson, and Alexandru Tatomir. Benchmarks for single-phase flow in fractured porous media. *Advances in Water Resources*, 111:239–258, 2018.

[6] Susanna Gebauer, Lina Neunhäuserer, Ralf Kornhuber, Steffen Ochs, Reinhard Hinkelmann, and Rainer Helmig. Equidimensional modelling of flow and transport processes in fractured porous systems i. In S. Majid Hassanizadeh, Ruud J. Schotting, William G. Gray, and George F. Pinder, editors, *Computational Methods in Water Resources*, volume 47 of *Developments in Water Science*, pages 335–342. Elsevier, 2002.

[7] Pierre Grisvard. *Elliptic problems in nonsmooth domains*. SIAM, 2011.

[8] Rainer Helmig et al. *Multiphase flow and transport processes in the subsurface: a contribution to the modeling of hydrosystems.* Springer-Verlag, 1997.

[9] Jürg Hunziker, Marco Favino, Eva Caspari, Beatriz Quintal, J Germán Rubino, Rolf Krause, and Klaus Holliger. Seismic attenuation and stiffness modulus dispersion in porous rocks containing stochastic fracture networks. *Journal of Geophysical Research: Solid Earth*, 123(1):125–143, 2018.

[10] Swedish Nuclear Power Inspectorate. The international hydrocoin project—background and results. *Organization for Economic Co-operation and Development, Paris*, 1987.

[11] Mohammad Karimi-Fard, Luis J Durlofsky, and Khalid Aziz. An efficient

discrete-fracture model applicable for general-purpose reservoir simulators. *SPE journal*, 9(02):227–236, 2004.

[12] Vincent Martin, Jérôme Jaffré, and Jean E Roberts. Modeling fractures and barriers as interfaces for flow in porous media. *SIAM Journal on Scientific Computing*, 26(5):1667–1691, 2005.

[13] Ali Moinfar, Abdoljalil Varavei, Kamy Sepehrnoori, and Russell T Johns. Development of an efficient embedded discrete fracture model for 3d compositional reservoir simulation in fractured reservoirs. *SPE Journal*, 19(02):289–303, 2014.

[14] Lina Neunhäuserer, Susanna Gebauer, Steffen Ochs, Reinhard Hinkelmann, Ralf Kornhuber, and Rainer Helmig. Equidimensional modelling of flow and transport processes in fractured porous systems ii. In S. Majid Hassanizadeh, Ruud J. Schotting, William G. Gray, and George F. Pinder, editors, *Computational Methods in Water Resources*, volume 47 of *Developments in Water Science*, pages 343–350. Elsevier, 2002.

[15] Martin Petzoldt. Regularity results for laplace interface problems in two dimensions. *Zeitschrift für Analysis und ihre Anwendungen*, 20(2):431–455, 2001.

[16] Tong Pin and Theodore H.H. Pian. On the convergence of the finite element method for problems with singularity. *International Journal of Solids and Structures*, 9(3):313–321, 1973.

[17] Tor Harald Sandve, Inga Berre, and Jan M Nordbotten. An efficient multi-point flux approximation method for discrete fracture–matrix simulations. *Journal of Computational Physics*, 231(9):3784–3800, 2012.

[18] Santiago G. Solazzi, Jürg Hunziker, Eva Caspari, J. Germán Rubino, Marco Favino, and Klaus Holliger. Seismic signatures of fractured porous rocks: The partially saturated case. *Journal of Geophysical Research: Solid Earth*, 125(8):e2020JB019960, 2020. e2020JB019960 10.1029/2020JB019960.